Supporting Information

Li^+-assisted treatment of graphene oxide for ultrahigh volumetric performance supercapacitor

Zhaoyuan Liu,[ab] Yue Yang,[c] Yinan Yuan,[d] Lidong Wang,*[a] Jie Sheng,*[e] Weidong Fei[af]

[a]*School of Materials Science and Engineering, Harbin Institute of Technology, Harbin 150001, P. R. China. E-mail: wld@hit.edu.cn, shengjie@hit.edu.cn*

[b]*College of Chemistry and Chemical Engineering, Harbin Normal University, Harbin 150025, P. R. China.*

[c]*Harbin Welding Institute Limited Company, Harbin 150028, P. R. China.*

[d]*School of Environmental and Chemical Engineering, Heilongjiang University of Science and Technology, Harbin 150022, P. R. China.*

[e]*Laboratory for Space Environment and Physical Science, Research Center of Basic Space Science, Harbin Institute of Technology, Harbin 150001, P. R. China.*

[f]*State Key Laboratory of Advanced Welding and Joining, Harbin Institute of Technology, Harbin 150001, P. R. China.*

Experimental section

Synthesis of materials: Graphite oxide was synthesized using a modified Hummers method 1. Natural graphite powder with an average size of 44 μm was purchased from Qingdao Jinrilai Graphite Co., Ltd. Briefly, a volume ratio of 9:1 mixture of concentrated H_2SO_4 (98%, 90 mL) and H_3PO_4 (85%, 10 mL) was added to the nature graphite powder (2 g) in ice-water bath. $KMnO_4$ (14 g) was gradually added with magnetic stirring, then the reactants were heated to 50 °C and stirred for 10 h. The reactants were cooled down to room temperature and distilled water (50 mL) was slowly added to cause an increase in temperature up to 95 °C, holding for 15 min and then a large amount of distilled water (450 mL) and 30% H_2O_2 solution (5 mL) were added to the reaction system. The product was washed by diluted hydrochloric acid and deionized water for several times. The GO colloid solution was vacuum-dried at 80 ºC for 12 h and denoted as GO-80.

Li^+-assisted heat treatment process: GO suspension (2 mg mL^{-1}, 100 mL) was treated by sonication for 2 h and then mixed with metal cationic chlorides LiCl. An appropriate amount of LiCl was added to the GO solution under the condition of magnetic stirring, so that the concentration of LiCl in the solution reached 3.5 mol L^{-1}. The solid-liquid separation was accomplished by centrifugation at 11 000 rpm for 15 min, and the precipitate was dried under vacuum (100 ºC, 12 h). The dried powder was put into a tube furnace and heat-treated at 400 ºC in an argon protective atmosphere for 60 min, with a heating rate of 10 ºC min^{-1} and a gas flow rate of 100 mL min^{-1}. The obtained sample was washed for 4 times by the mixture of water and ethanol (water/ethanol = 60/40 vol. %) and dried at 80 ºC for 4 h. The obtained reduced graphene oxide was named as Li-RGO-400. As a comparison, GO was also heat treated without LiCl, the obtained sample denoted as Ar-RGO-400. To investigate the influence of heat treatment temperature, 100 ºC, 200 ºC, 300 ºC, 500 ºC and 600 ºC were also selected to carry out the Li^+-assisted heat treatment process.

Characterizations: The microstructure and morphology were examined by environmental scanning electron microscopy (ESEM, Zeiss Merlin Compact) and high-resolution transmission electron microscopy (HRTEM, JEM-2100F). The X-ray photoelectron spectroscopy (XPS) characterization of the products was executed on Thermo Fisher Scientific Esca Xi^+ spectrometer with an Al Kα (*hv*=1486.69 eV) X-ray source. The powder X-ray diffraction (XRD) measurements were carried out on a Philips X'pert diffractometer with Cu Kα irradiation (λ=1.54 Å). The Raman spectra were recorded using a B&WTEK spectrometer (BWS435-532SY) with a 532 nm laser (*hv*=2.34 eV), 2% laser power (total power: 240 mW). The FTIR spectra were recorded in KBr pellets using a WQF-530 FTIR spectrometer in the wavenumber region 4000 to 400 cm^{-1}. The N_2 adsorption/desorption isotherms were measured using an ASAP2460/Autochem2920 analyzer. The specific surface area and pore size distribution were determined by Brunauer-Emmett-Teller (BET) and Barrett-Joyner-Halenda (BJH) desorption analyses, respectively. The packing density ρ of RGOs was calculated through the following equation 2, 3:

$$\rho = \left(V_{\text{total}} + 1/\rho_{\text{carbon}}\right)^{-1} \qquad \backslash* \text{ MERGEFORMAT (1)}$$

where ρ is the packing density of the materials and the ρ_{carbon} is the true density of carbon (2 g cm^{-3}), V_{total} is the total pore volume estimated from N_2 isotherm at 77 K.

Electrochemical measurements: The electrochemical experiments were carried out using a conventional three- and two-electrode system with an aqueous system (electrolyte: 1 M H_2SO_4) using CHI760D electrochemical workstation. Three-electrode cells were used to evaluate the Faradaic processes and the available potential window, and two-electrode cells were constructed to simulate actual device behavior. The working electrode was prepared by mixing the active materials with polyvinylidene fluoride (PVDF) and acetylene black with a weight ratio of 80:10:10 in N-methyl-2-pyrrolidone (NMP) until homogeneous slurry was formed. The as-prepared slurry was dropped onto the stainless-steel mesh (300 mesh) with areal

of 1 cm^2, with active mass loading of 2~3 mg cm^{-2}. The electrode was dried at 120 °C in a vacuum oven for 10 h. After then, the electrode was pressed under 10 MPa for 2 minutes to improve the packing density. The Ag/AgCl ($KCl_{sat.}$) electrode and a slice of platinum served as reference and counter electrodes, respectively. For all the samples, before formally starting the electrochemical test, the activation was performed at the scan rate of 100 mV s^{-1} for 200 cycles to stabilize the electrode. The cyclic voltammetry (CV) tests were investigated between -0.2 V and 0.9 V (*vs.* Ag/AgCl). The galvanostatic charge/discharge (GCD) was performed in the same potential range at the current densities ranging from 0.1 to 50 A g^{-1}. GCD was assumed to be the most accurate technique especially for redox supercapacitor. The electrochemical impendence spectroscopy (EIS) measurements were evaluated in the frequency range from 100 kHz to 0.01 Hz at open circuit potential with an ac perturbation of 5 mV. The simulation of the experiment impedance using three-electrode data was carried out with Zview software.

Fabrication of supercapacitors: As for the fabrication of the two-electrode symmetric supercapacitor systems, two electrodes with exactly the same mass were assembled in CR2025 stainless steel coin-type cells with the porous cellulose membrane as separator and 1 M H_2SO_4 aqueous solution as electrolyte.

Calculation of the specific capacitances: The measured specific capacitance of the current collector (stainless-steel mesh) is about 0.064 F g^{-1} @ 5 mV s^{-1}, which is much less than the typical capacitance of graphene (50 ~ 300 F g^{-1}). Therefore, the influence of current collector is neglectable.

(1) Three-electrode configuration

The gravimetric specific capacitances based on the active material (C_g, F g^{-1}) were calculated according to the GCD curves at different current densities:

$$C_g = \frac{I\Delta t}{m\Delta U} \qquad \text{* MERGEFORMAT (2)}$$

where I is the discharge current (A), Δt is the discharge time (s), m is the weight of the active

material (g), and ΔU is the discharge voltage (V) excluding the internal resistance (iR) drop during the discharge process.

The volumetric performances of the active materials (C_V, F cm^{-3}) were calculated according to the following equation:

$$C_V = C_g \rho \qquad \text{* MERGEFORMAT (3)}$$

where C_g presents the gravimetric capacitance of the active material, ρ is the packing density (g cm^{-3}) of the active material.

(2) Two-electrode configuration

The gravimetric specific capacitance of the device was calculated by the following equation:

$$C_{g\text{-}2e} = \frac{I\Delta t}{2m\Delta U} \qquad \text{* MERGEFORMAT (4)}$$

where I is the discharge current (A), Δt is the discharge time (s), m is the weight of the active material in the individual electrode (g), and ΔU is the discharge voltage (V) excluding the iR drop during the discharge process.

The energy densities (E) and power density (P) of the symmetric cell were estimated according to the following equation:

$$E = \frac{1}{2} C \times \Delta U^2 \qquad \text{* MERGEFORMAT (5)}$$

$$P = \frac{E}{t} \qquad \text{* MERGEFORMAT (6)}$$

Where C represents the gravimetric/areal/volumetric capacitance based on the two-electrode system. ΔU is the discharge voltage excluding the iR drop during the discharge process, and t is the discharging time measured in the galvanostatic charging and discharging experiments.

Calculation of the coulombic efficiency and energy efficiency: The coulombic efficiency (η_c) was calculated by the following equation:

$$\eta_c = \frac{t_D}{t_C} \times 100\% \qquad \text{* MERGEFORMAT (7)}$$

Where t_D and t_C is the discharge duration time and charge duration time.

The energy efficiency (η_e) was calculated by the following equation:

$$\eta_e = \frac{E_D}{E_C} \times 100\% \qquad \text{* MERGEFORMAT (8)}$$

where E_D is discharge specific energy obtained by discharge curve integrating and E_C is charge specific energy obtained by charge curve integrating, as shown in the following equations

$$E_D = I\int U(t_D)dt_D \qquad \text{* MERGEFORMAT (9)}$$

$$E_C = I\int U(t_C)dt_C \qquad \text{* MERGEFORMAT (10)}$$

Supplementary Fig. S1-Fig. S19 and Table S1-Table S5

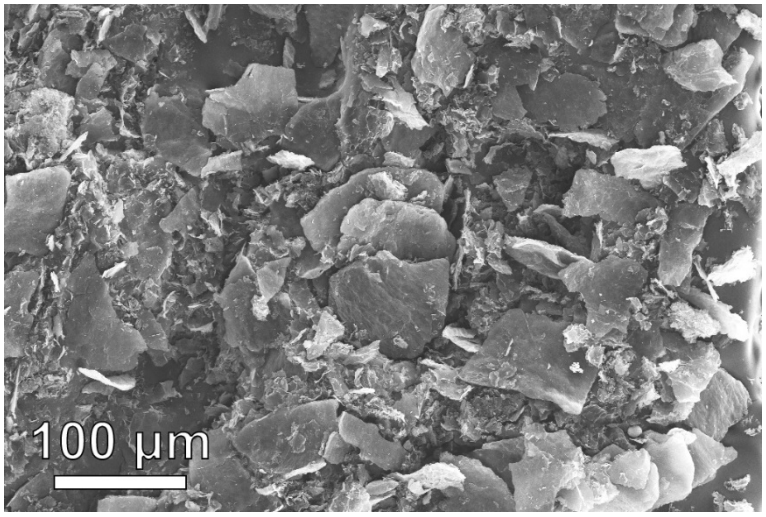

Fig. S1 The SEM image of Li-RGO-400.

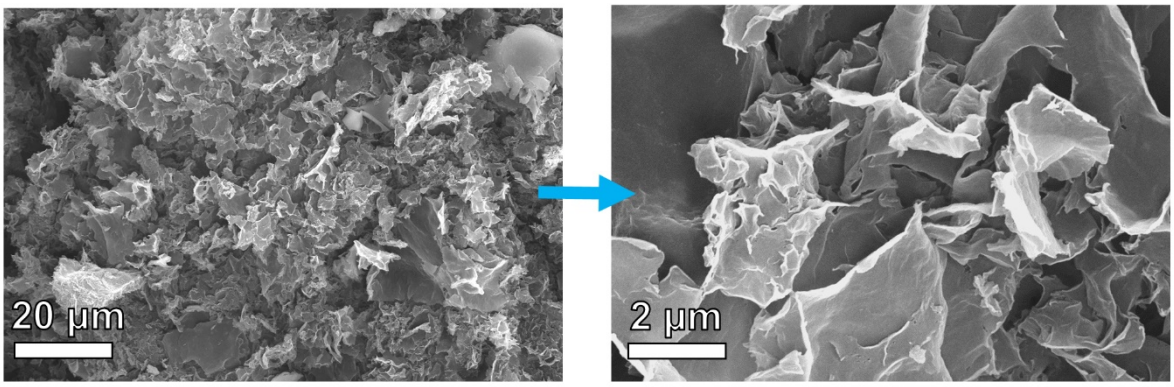

Fig. S2 SEM images of Li-RGO-400 with the LiCl concentration of 19.7 mol L^{-1}.

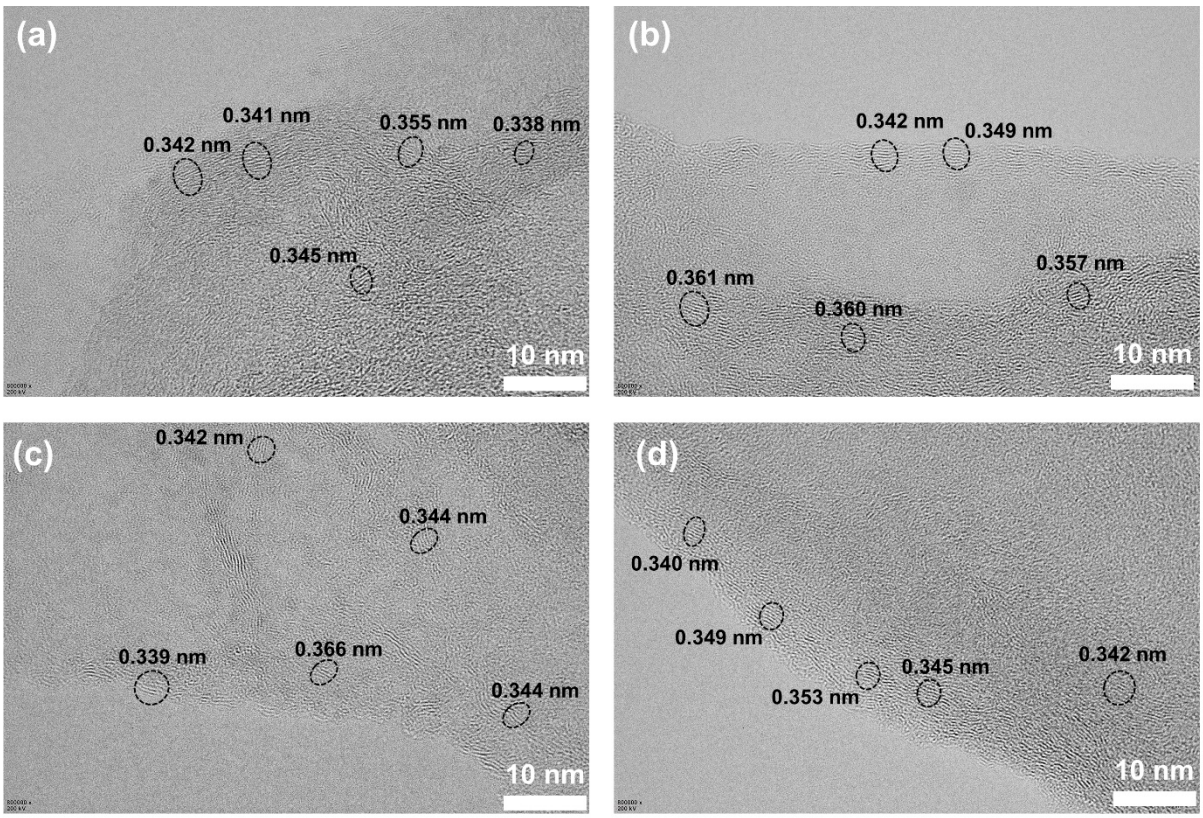

Fig. S3 (a)-(d) HRTEM images of Li-RGO-400 at different regions

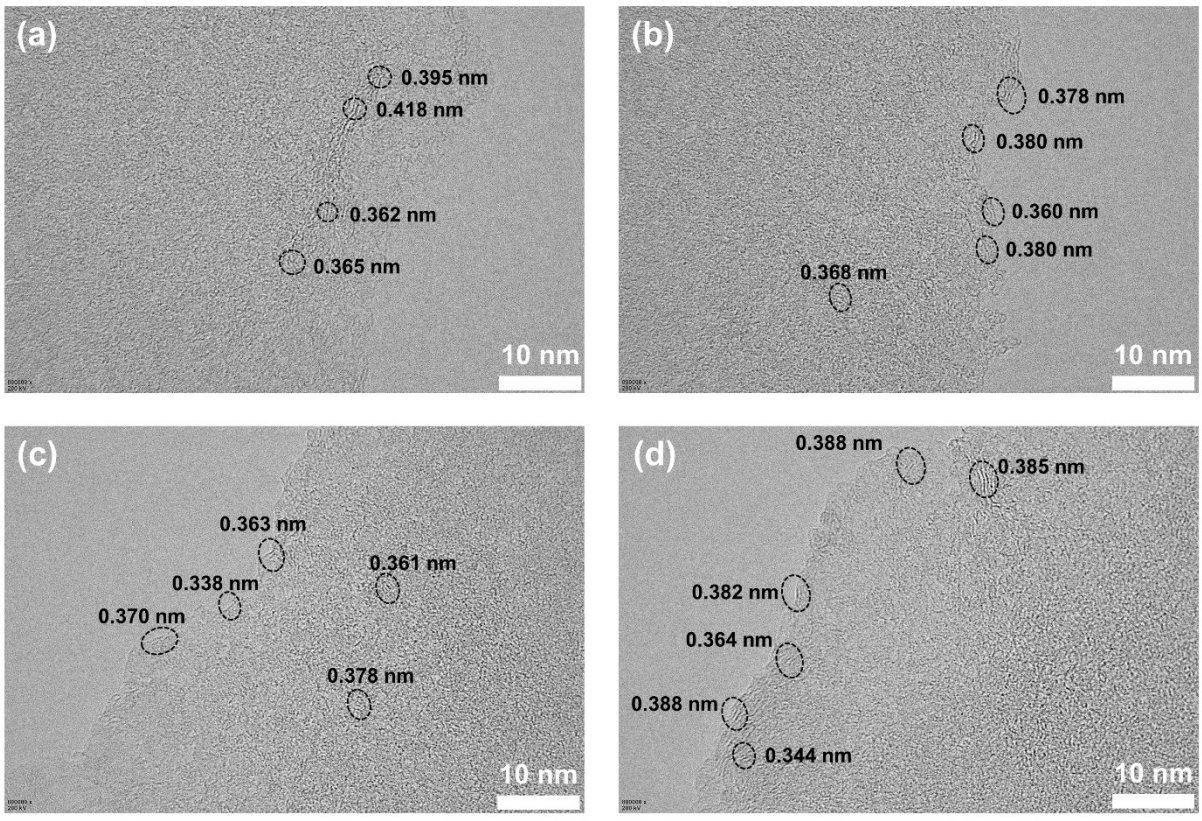

Fig. S4 (a)-(d) HRTEM images of Ar-RGO-400 at different regions

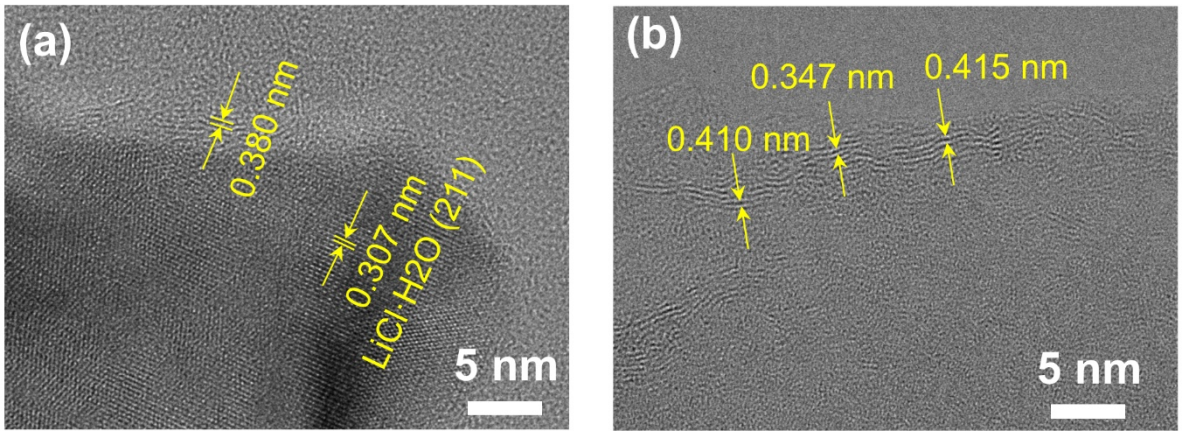

Fig. S5 TEM images of Li-RGO-400 before washing.

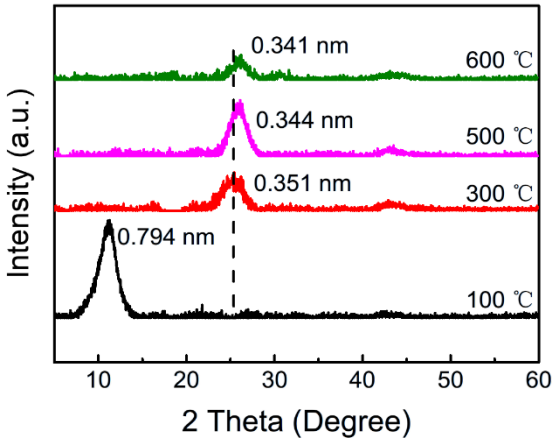

Fig. S6 XRD spectra of Li-RGOs prepared at different heat treatment temperatures.

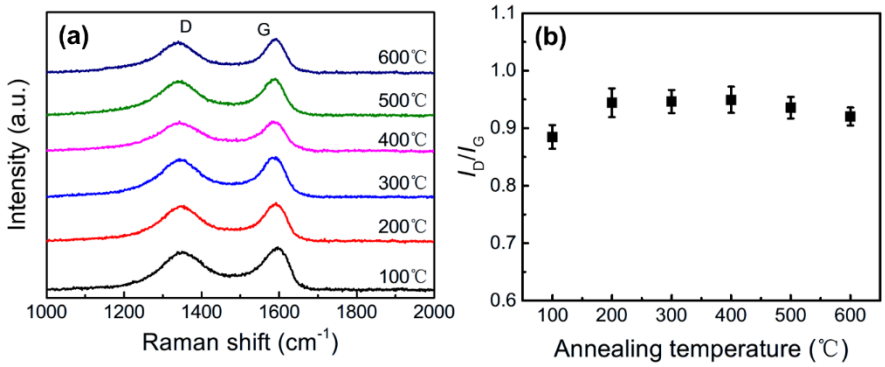

Fig. S7 (a) Raman spectra of Li-RGOs prepared with different heat treatment temperature. (b) The relationship of I_D/I_G ratio with annealing temperature.

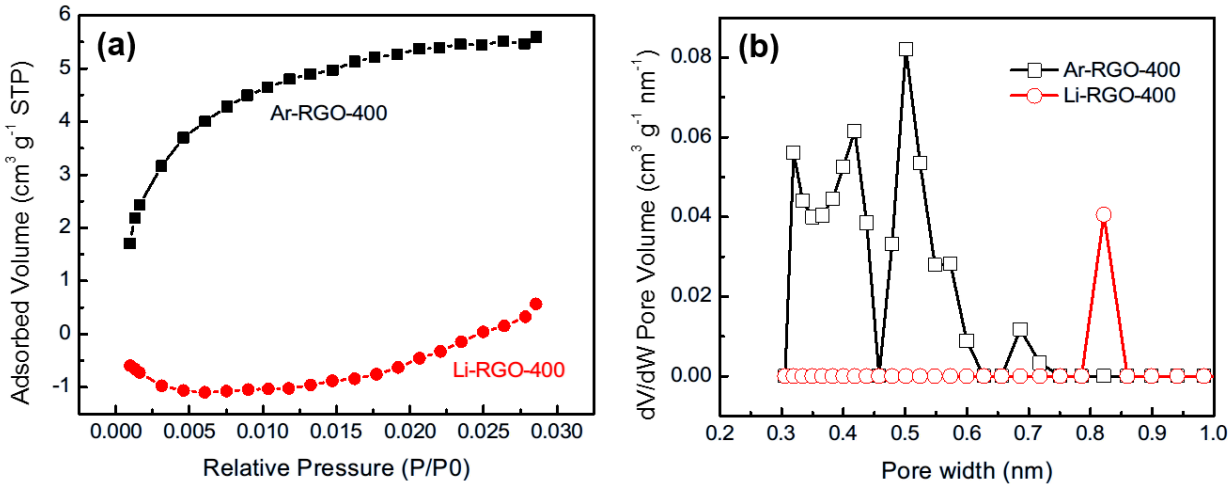

Fig. S8 (a) CO_2 adsorption isotherms of Ar-RGO-400 and Li-RGO-400. (b) Pore-size distribution calculated by nonlocal density functional density (NLDFT) model.

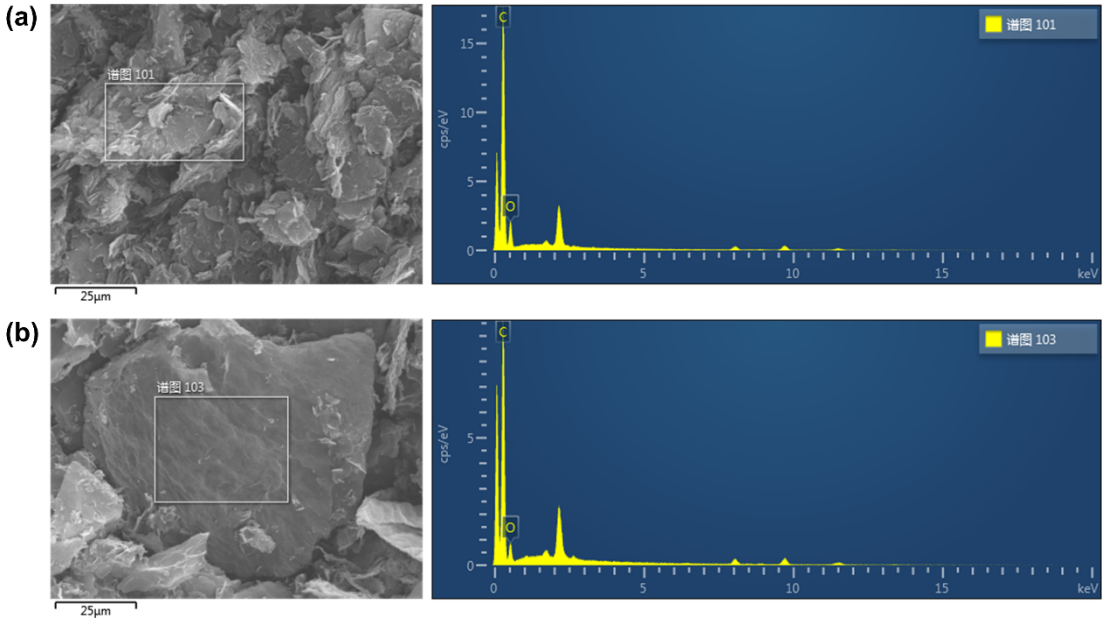

Fig. S9 The EDS spectra of (a) Ar-RGO-400 and (b) Li-RGO-400. The O content of Li-RGO-400 and Ar-RGO-400 are 15.37 at.% and 18.99 at.%, respectively.

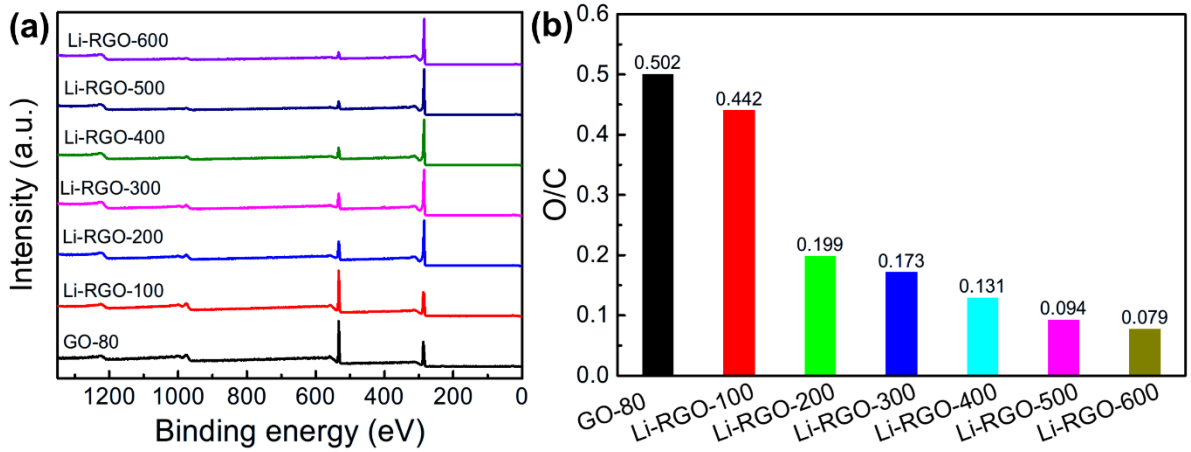

Fig. S10 (a) XPS surveys and (b) O/C ratios of Li-RGOs prepared at different heat treatment temperature.

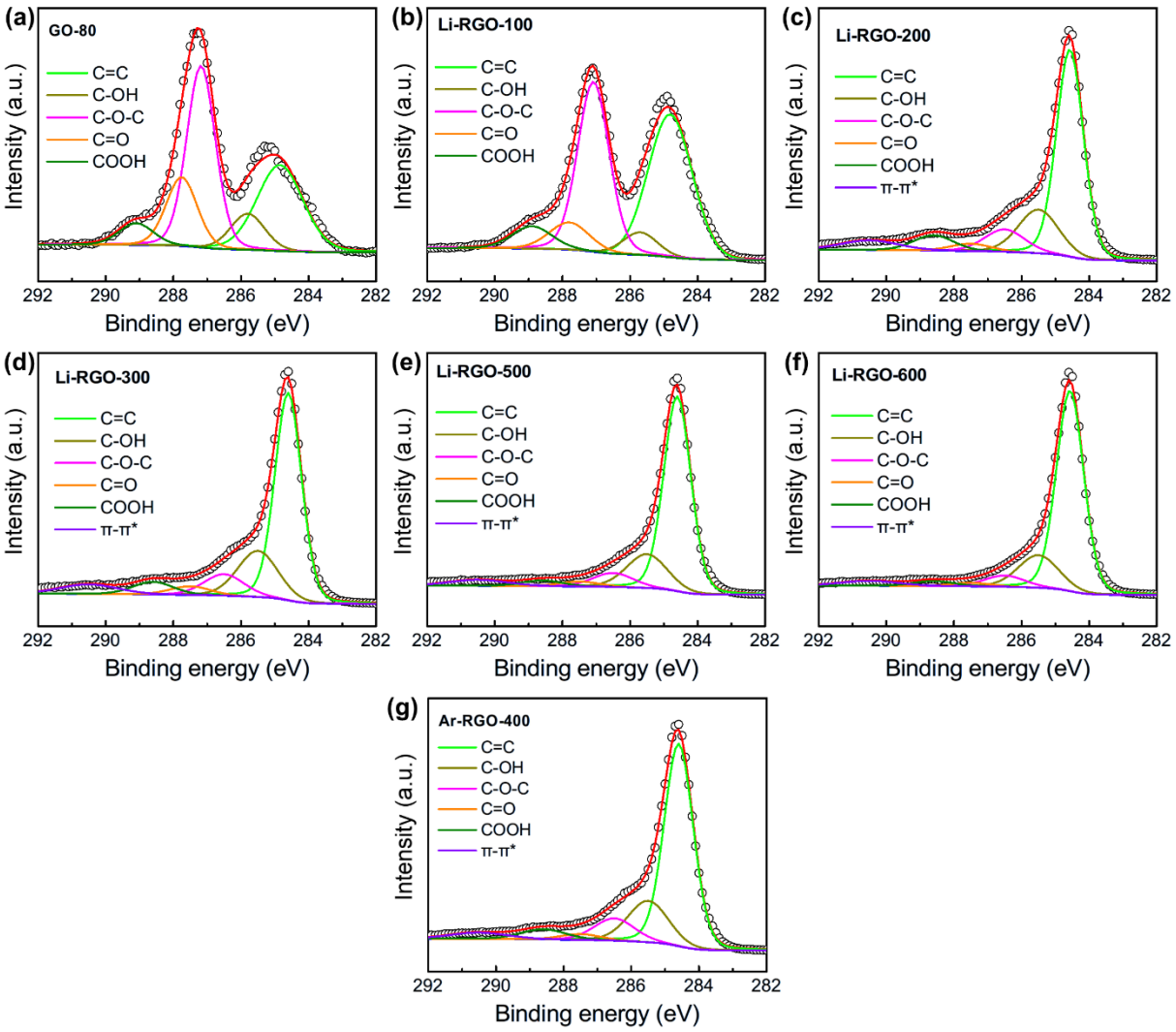

Fig. S11 (a) C 1s high-resolution spectra of Li-RGOs prepared at different heat treatment

temperatures.

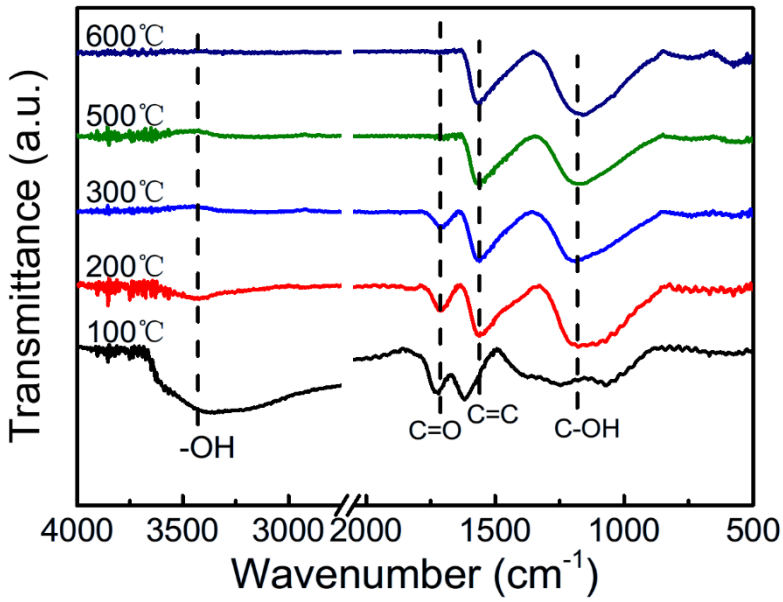

Fig. S12 The FTIR spectrum of Li-RGOs prepared with different heat treatment temperature.

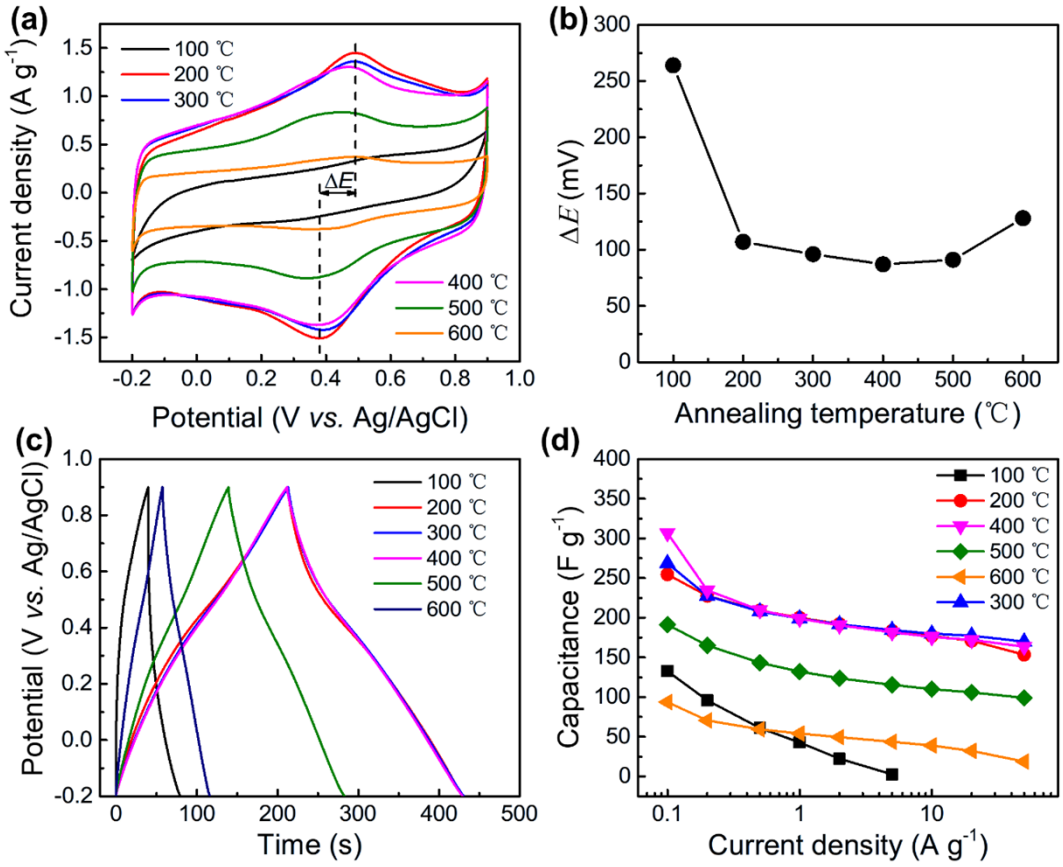

Fig. S13 (a) CV curves comparison of Li-RGOs at 5 mV s^{-1}. (b) Relationships of separation of redox peaks ΔE with the annealing temperatures. (c) GCD curves comparison of Li-RGOs at 1

A g^{-1}. (d) Comparison of the specific capacitance of Li-RGOs at various current densities.

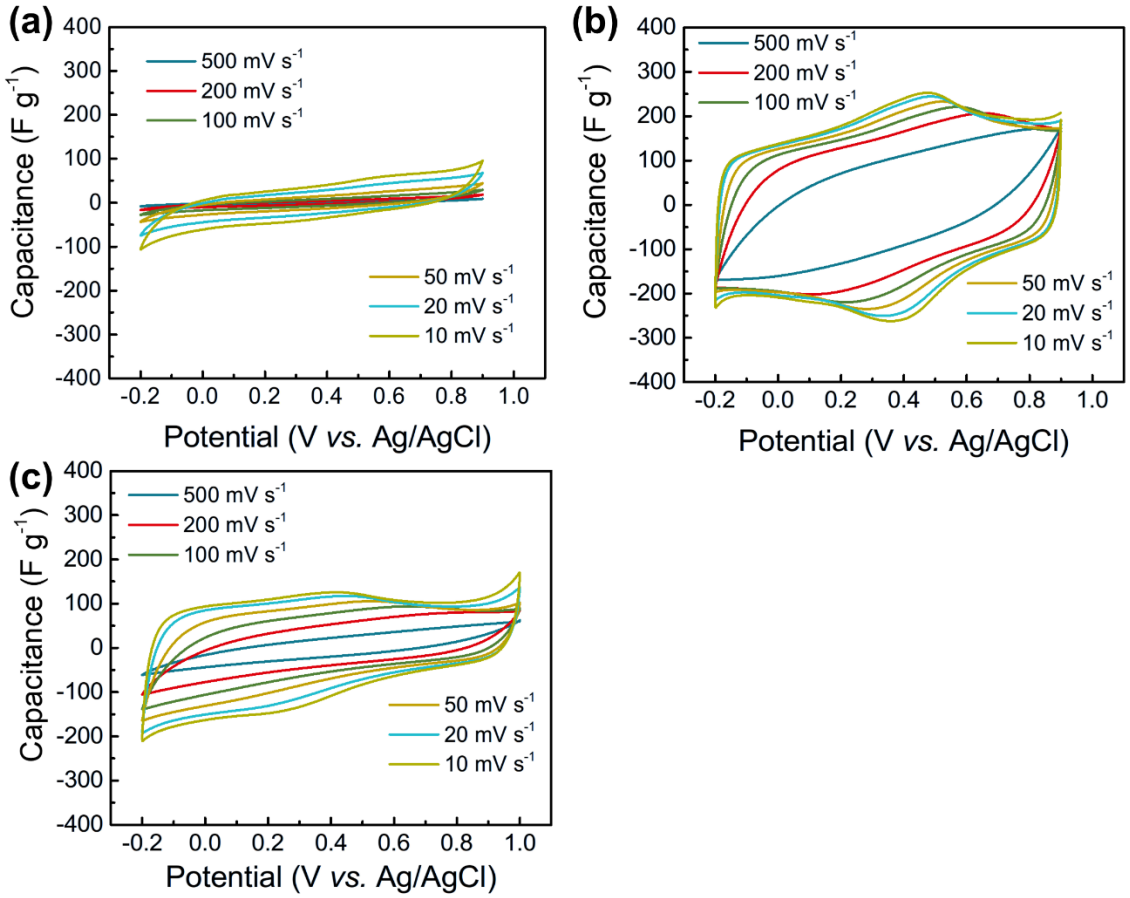

Fig. S14 CV curves of (a) Li-RGO-400 and (b) Ar-RGO-400 at different scan rates.

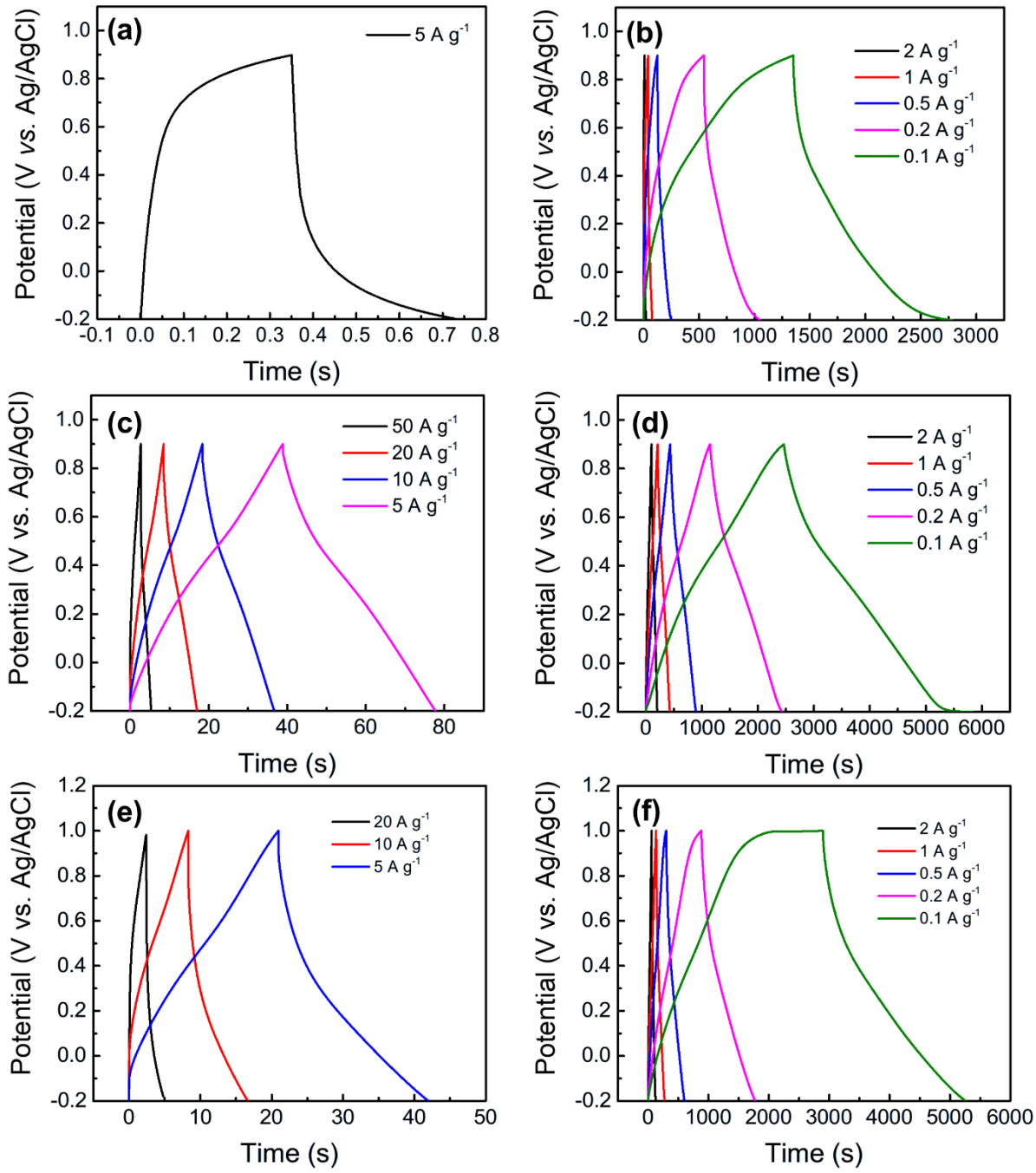

Fig. S15 (a)-(b) GCD curves of GO-80 at different current densities. (c)-(d) GCD curves of Li-RGO-400 at different current densities. (e)-(f) GCD curves of Ar-RGO-400 at different current densities.

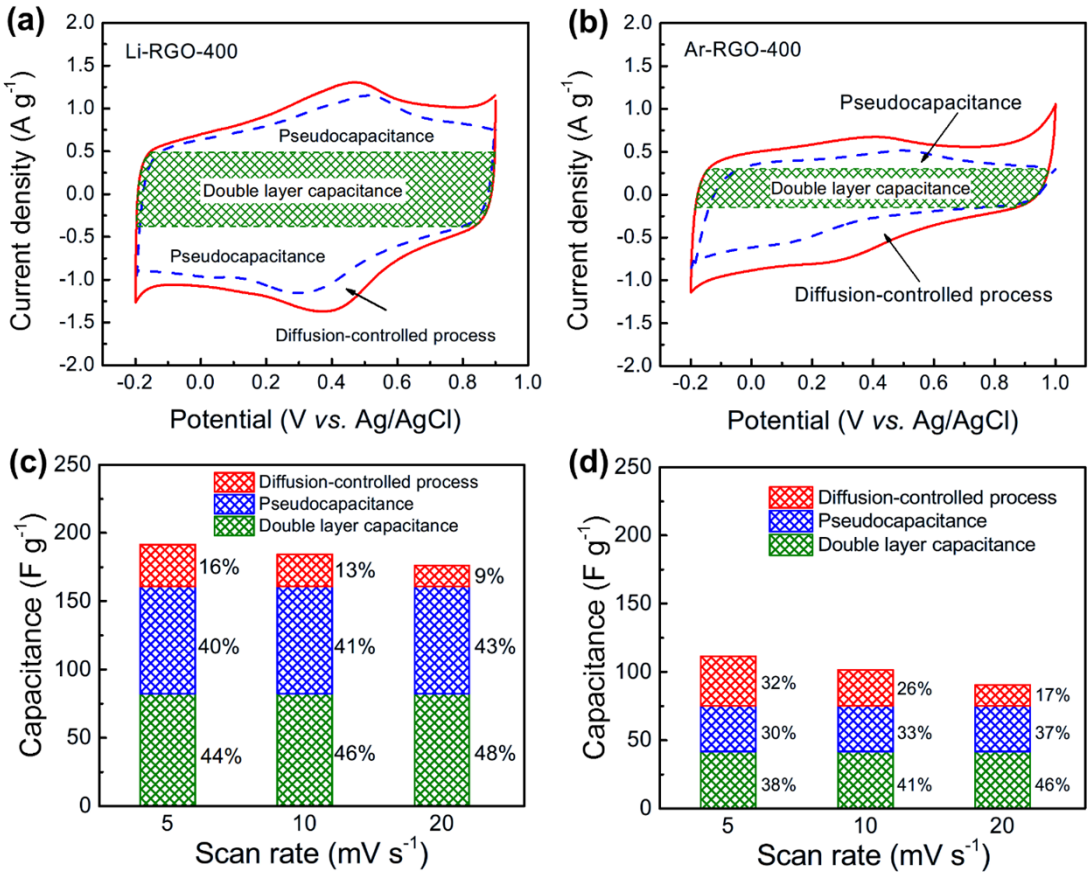

Fig. S16 The mechanisms of charge storage. Decoupling of the capacitance contributed by double layer capacitance, pseudocapacitance and diffusion-controlled process of (a) Li-RGO-400 and (b) Ar-RGO-400. Histograms of the capacitance contributions at different scan rates of (c) Li-RGO-400 and (d) Ar-RGO-400.

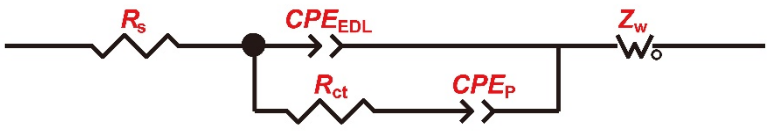

Fig. S17 The equivalent electric circuit model used for fitting the Nyquist plots. R_s: the intrinsic ohmic resistance; R_{ct}: charge transfer resistance; CPE_{EDL}: constant phase element representing the electrical double layer capacitance (EDLC); CPE_P: constant phase element representing the pseudocapacitance provided by the oxygen functional groups; Z_w: a Generalized Finite Warburg element terminating in an open circuit. The specific values for each component were listed in Table S4.

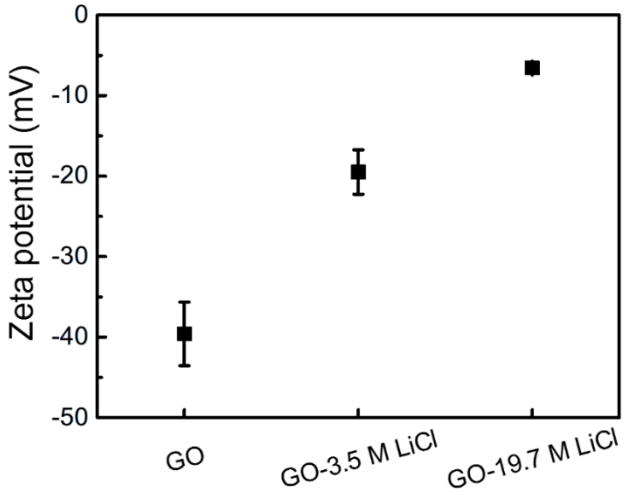

Fig. S18 Zeta potential of GO and GO with addition LiCl.

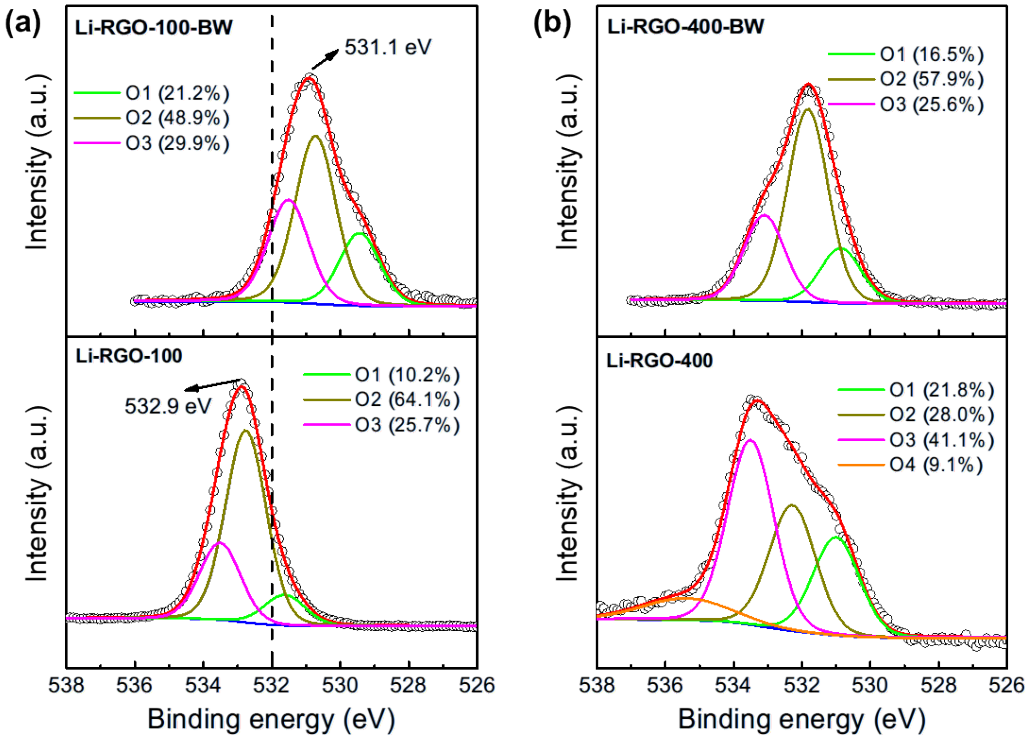

Fig. S19 The evidences of interactions of metal cations with graphene. (a) The O 1s high resolution spectra of Li-RGO-100 before (top plane) and after (bottom plane) washing off LiCl. (b) The O 1s high resolution spectra of Li-RGO-400 before (top plane) and after (bottom plane) washing off LiCl.

The interaction of Li^+ with OFGs can be demonstrated by O 1s spectra in XPS. Fig. S19 displays the O 1s fine plots of Li-RGO-100 and Li-RGO-400 samples before and after removal

of LiCl, all the peak positions were corrected with C 1s = 284.6 eV. In the case of Li-RGO-100, the main O 1s peak position locates at 532.9 eV, as shown in bottom plane in Fig. S19a. However, the peak position before water washing (Li-RGO-100-BW) was down-shifted to 531.1 eV, as shown in top plane. This down-shift of the binding energy of O 1s may be due to the interaction of Li^+ with the OFGs, resulting in a lower binding energy between the oxygen and carbon atom. 4 Furthermore, O 1s high-resolution spectra unveil the protection mechanism of Li^+ to C-OH group. The O 1s high-resolution spectrum can be divided into four peaks: O1 corresponding to C=O or Li-O, O2 corresponding to C-O-C or C-O-Li, 5 O3 corresponding to C-OH, and O4 corresponding to oxygen around the vacancies on the graphene basal plane. Some C=O and C-OH were converted to C-O-Li as the heat temperature increased from 100 ºC to 400 ºC, demonstrating by the comparison of the O1s spectra of Li-RGO-400-BW and Li-RGO-100-BW. After washing, the relative content of C-OH increased in Li-RGO-400 as shown in Fig. S19b, which can be attributed to the hydrolysis reaction of C-O-Li.

Table S1 The parameters of specific surface area and total pore volume calculated from nitrogen adsorption measurements.

Samples	BET SSA ($m^2\ g^{-1}$)	Total pore volume ($cm^3\ g^{-1}$)	Packing density ($g\ cm^{-3}$)
GO-80	144	0.156	1.52
Ar-RGO-400	331	0.626	0.89
Li-RGO-400	87	0.099	1.67

Table S2 The contents of oxygen functional groups of GO-80 and Li-RGOs estimated by the XPS area in C 1s peak. (Unit: at.%)

Samples	C=C	C-OH	C-O-C	C=O	HO-C=O	π-π*
GO-80	29.7	9.3	39.3	16.0	5.6	--
Li-RGO-100	42.3	5.5	38.0	7.8	6.4	--
Li-RGO-200	57.6	18.1	9.3	3.1	6.3	5.6
Li-RGO-300	57.4	19.2	8.9	3.6	5.2	5.7
Li-RGO-400	61.0	19.5	7.9	3.1	3.9	4.6
Li-RGO-500	66.2	17.1	7.0	2.5	2.9	4.3
Li-RGO-600	69.6	16.7	5.7	1.8	2.6	3.6

Table S3 Comparison of the rate stability of Li-RGO-400 with other reported carbon-based materials

Materials	Electrolyte	Scan rate or current density	Capacitance ($F g^{-1}$)	Rate capability	Reference
CNC700	1M H_2SO_4	0.1 A g^{-1}	260	43% @ 100 A g^{-1}	6
IPGEs	1M H_2SO_4	10 mV s^{-1}	132	36% @ 500 mV s^{-1}	7
HCP	1M H_2SO_4	1 A g^{-1}	140	40% @ 64 A g^{-1}	8
PrGO-IL	1M H_2SO_4	0.5 A g^{-1}	262	67% @ 20 A g^{-1}	9
FG1.3	1M H_2SO_4	1 A g^{-1}	279	54% @ 100 A g^{-1}	10
aGA-0.5	1M H_2SO_4	0.2 A g^{-1}	204	69% @ 30 A g^{-1}	11
RGO-MP40	1M H_2SO_4	0.1 A g^{-1}	312	66% @ 50 A g^{-1}	12
Ar-RGO-400	1M H_2SO_4	0.1 A g^{-1}	198	34%@20 A g^{-1}	**This work**
Li-RGO-400	1M H_2SO_4	0.1 A g^{-1}	303	56%@20 A g^{-1}	

Table S4 The specific values for each component of the fitted electric circuit model

Element	Ar-RGO-400	Li-RGO-400
R_s, /ohm	0.8232	0.9288
CPE_{EDL}-T	0.0007	0.0015
CPE_{EDL}-P	0.8827	0.8635
R_{ct}, /ohm	1.5460	0.0122
CPE_P-T	10.5900	0.0709
CPE_P-P	1.4850	0.0107
Z_w-R, /ohm	11.0600	0.0475
Z_w-T	1.3960	0.2354
Z_w-P	0.4178	0.0150

Table S5 The electrochemical performance of representative carbon electrodes.

Material	Mass loading (mg cm^{-2})	Packing density (g cm^{-3})	Current density	Gravimetric capacitance (F g^{-1})	Volumetric capacitance (F cm^{-3})	Electrode configuration	Electrolyte	Reference
Li-RGO-400	**3**	**1.67**	**0.1 A g^{-1}**	**307**	**512**	**3 electrode**	**1 M H_2SO_4**	**This work**
3D carbon composite	56.9	0.256	10 mV s^{-1}	161	41.3	3 electrode	6 M KOH	13
N-doped graphene film	0.32	1.64	1 A g^{-1}	252	413	2 electrode	1 M H_2SO_4	14
	11.2	1.64	1 A g^{-1}	226	370	2 electrode	1 M H_2SO_4	
rGO/SWCNT film	6.2	1.59	114 mA cm^{-3}	255	407	2 electrode	H2SO4/PVA	15
Multilayered-folded graphene nanoribbon film	21	0.92	5 mA cm^{-2}	318	293	3 electrode	6 M KOH	16
Activated wood carbon	30	0.38	1 mA cm^{-2}	118.7	44.8	3 electrode	1 M Na_2SO_4	17
Activated Carbon/Graphene Hybrid Aerogels	~10	0.58	0.05 A g^{-1}	294	170.5	2 electrode	6 M KOH	18
N- and O-enriched porous carbon/graphene composites	3	0.47	0.1 A g^{-1}	380	178	2 electrode	6 M KOH	19
Nitrogen-Doped Mesoporous Carbons	4.0	1.36	0.1 A g^{-1}	147	200	2 electrode	1 M H_2SO_4	20
carbon/graphene nanofibers@graphene composite cloth	3	1.2	0.2 A g^{-1}	241	294	3 electrode	6 M KOH	21
nitrogen-enriched porous carbon/graphene	3	1.08	0.05 A g^{-1}	339	365	2 electrode	6 M KOH	22
Nitrogen-doped graphene	2.0	1.31	0.5 A g^{-1}	334	437.5	3 electrode	6 M KOH	23
nitrogen doped holey graphene	2.0	1.30	0.1 A g^{-1}	375	439	3 electrode	6 M KOH	24
graphene films	0.8	1.6	1 A g^{-1}	340	326	3 electrode	1 M H_2SO_4	25

Material	Mass loading (mg cm^{-2})	Packing density (g cm^{-3})	Current density	Gravimetric capacitance (F g^{-1})	Volumetric capacitance (F cm^{-3})	Electrode configuration	Electrolyte	Reference
	2.84	0.11	1 A g^{-1}	213	25.41	3 electrode	1 M H_2SO_4	
nitrogen-doped active carbon/ graphene composites	3	0.68	0.05 A g^{-1}	378.9	257.7	3 electrode	6 M KOH	26
Reduced Graphene Oxide Hydrogels	1.92	1.32	1 A g^{-1}	133.7	176.5	2 electrode	6 M KOH	27
carbon quantum dots	5.16	1.23	0.5 A g^{-1}	128	157.4	2 electrode	6 M KOH	28
holey reduced graphene oxide	1.5	0.86	1 A g^{-1}	251	216	3 electrode	6 M KOH	29
holey graphene oxide	1.0	1.12	1 A g^{-1}	209	234	2 electrode	1 M H_2SO_4	30
Functional Pillared Graphene Frameworks	2	1.5	2 mV s^{-1}	353	400	3 electrode	6 M KOH	31
carbon hollow submicron spheres	0.2	0.87	0.2 A g^{-1}	386	335	3 electrode	6 M KOH	32
graphene nanomesh-carbon nanotube hybrid film	0.5	1.13	5 mV s^{-1}	294	331	3 electrode	6 M KOH	33
Holey graphene frameworks	1	0.71	1 A g^{-1}	310	220	2 electrode	6 M KOH	34
Crumpled graphene balls	20	0.5	0.1 A g^{-1}	150	75	2 electrode	5 M KOH	35
Liquid-mediated chemically converted graphene	1	1.33	0.1 A g^{-1}	191.7	255.5	2 electrode	1 M H_2SO_4	36
	1	1.33	0.1 A g^{-1}	196.5	261.3	2 electrode	EMIMBF$_4$/AN	
	10	1.25	0.1 A g^{-1}	164	205	2 electrode	EMIMBF$_4$/AN	
reduced graphene oxide fiber fabrics	9	0.41	1 mA cm^{-2}	285	117	3 electrode	1 M H_2SO_4	37
EGM-rGO film	15	0.94	1 A g^{-1}	201	189	2 electrode	EMIMBF$_4$	38

Material	Mass loading (mg cm^{-2})	Packing density (g cm^{-3})	Current density	Gravimetric capacitance (F g^{-1})	Volumetric capacitance (F cm^{-3})	Electrode configuration	Electrolyte	Reference
Highly ordered and compact porous carbon	2	1.48	0.1 A g^{-1}	255	378	3 electrode	1 M $ZnSO_4$	39
Highly ordered graphene solid (HOGS)	2	1.48	0.05 A g^{-1}	205	303	3 electrode	1M NaClO4	40
Reduced pillared graphene materials	--	1.10	10 mV s^{-1}	200	210	2 electrode	TEABF4/AN	41
Ultramicroporous carbons (CoDCs)	2	0.97	1 A g^{-1}	270	262	3 electrode	6 M KOH	42
YP80/G	--	0.76	0.2 A g^{-1}	181	138	2 electrode	1 M EMIMBF4/AN	43
N doped graphene microspheres	1.5	1.4	0.1 A g^{-1}	185	259	2 electrode	1 M EMIMBF4/AN	44
Cabbage-like graphene (C-GR) microsphere	2.5	0.75	0.1 A g^{-1}	177	117	2 electrode	5 M KOH	45
Electrostatic densified activated carbon (EDAC)	2	0.75	1 A g^{-1}	341	256	3 electrode	6 M KOH	46
Lignin-Derived Carbon nanofibers	3	0.6	0.1 A g^{-1}	200	130	2 electrode	6 M KOH	47
Sulfur-templated graphene assemblies (STGAs)	--	0.72	1 A g^{-1}	150	108	2 electrode	ionic liquid (IL)	48
Defect-enriched graphene block DGB	2	0.917	1 A g^{-1}	235	215	3 electrode	6 M KOH	49
Strutted nitrogen doped hierarchical porous carbon nanosheets (SNPCNS)	2	1.11	1 A g^{-1}	355	394	3 electrode	1 M H2SO4	50

Supplementary References

1. D. C. Marcano, D. V. Kosynkin, J. M. Berlin, A. Sinitskii, Z. Sun, A. Slesarev, L. B. Alemany, W. Lu and J. M. Tour, *ACS Nano*, 2010, **4**, 4806-4814.
2. F. Yue, G. Gao, F. Li, Y. Zheng and S. Hou, *Carbon*, 2018, **134**, 112-122.
3. J. Yan, Q. Wang, T. Wei, L. L. Jiang, M. L. Zhang, X. Y. Jing and Z. J. Fan, *Acs Nano*, 2014, **8**, 4720-4729.
4. H. Zhou and D. Zhang, *J Phys Chem Solids*, 2021, **154**.
5. R. Tatara, P. Karayaylali, Y. Yu, Y. Zhang, L. Giordano, F. Maglia, R. Jung, J. P. Schmidt, I. Lund and Y. Shao-Horn, *Journal of The Electrochemical Society*, 2018, **166**, A5090-A5098.
6. K. Xie, X. T. Qin, X. Z. Wang, Y. N. Wang, H. S. Tao, Q. Wu, L. J. Yang and Z. Hu, *Adv. Mater.*, 2012, **24**, 347-352.
7. L. T. Le, M. H. Ervin, H. W. Qiu, B. E. Fuchs and W. Y. Lee, *Electrochem. Commun.*, 2011, **13**, 355-358.
8. D. Salinas-Torres, R. Ruiz-Rosas, M. J. Valero-Romero, J. Rodriguez-Mirasol, T. Cordero, E. Morallon and D. Cazorla-Amoros, *J. Power Sources*, 2016, **326**, 641-651.
9. T. T. Li, N. Li, J. W. Liu, K. Cai, M. F. Foda, X. M. Lei and H. Y. Han, *Nanoscale*, 2015, **7**, 659-669.
10. F. Liu and D. F. Xue, *Chem. Eur. J.*, 2013, **19**, 10716-10722.
11. X. X. Sun, P. Cheng, H. J. Wang, H. Xu, L. Q. Dang, Z. H. Liu and Z. B. Lei, *Carbon*, 2015, **92**, 1-10.
12. Z. Liu, L. Wang, G. Ma, Y. Yuan, H. Jia and W. Fei, *J. Mater. Chem. A*, 2020, **8**, 18933-18944.
13. T. T. Gao, Z. Zhou, J. Y. Yu, J. Zhao, G. L. Wang, D. X. Cao, B. Ding and Y. J. Li, *Adv. Energy Mater.*, 2019, **9**, 1802578.
14. T. Q. Huang, X. Y. Chu, S. Y. Cai, Q. Y. Yang, H. Chen, Y. J. Liu, K. Gopalsamy, Z. Xu, W. W. Gao and C. Gao, *Energy Storage Materials*, 2019, **17**, 349-357.
15. J. Zhong, W. Sun, Q. Wei, X. Qian, H. M. Cheng and W. Ren, *Nat. Commun.*, 2018, **9**, 3484.
16. L. Z. Sheng, J. Chang, L. L. Jiang, Z. M. Jiang, Z. Liu, T. Wei and Z. J. Fan, *Adv. Funct. Mater.*, 2018, **28**, 1800597.
17. C. Chen, Y. Zhang, Y. Li, J. Dai, J. Song, Y. Yao, Y. Gong, I. Kierzewski, J. Xie and L. Hu, *Energy Environ. Sci.*, 2017, **10**, 538-545.
18. Q. Z. Zhu, L. Ma, H. R. Wang, M. Q. Jia, Y. B. Guan and B. Xu, *Chemistryselect*, 2017, **2**, 4456-4461.
19. S. W. Zhou, Q. X. Xie, S. H. Wu, X. L. Huang and P. Zhao, *Ionics*, 2017, **23**, 1499-1507.
20. X. Q. Yang, H. Ma and G. Q. Zhang, *Langmuir*, 2017, **33**, 3975-3981.
21. Q. X. Xie, S. W. Zhou, S. H. Wu, Y. F. Zhang and P. Zhao, *Applied Surface Science*, 2017, **407**, 36-43.

22. Q. X. Xie, G. H. Chen, R. R. Bao, Y. F. Zhang and S. H. Wu, *Microporous and Mesoporous Materials*, 2017, **239**, 130-137.
23. X. Zhao, H. W. Dong, Y. Xiao, H. Hu, Y. J. Cai, Y. R. Liang, L. Y. Sun, Y. L. Liu and M. T. Zheng, *Electrochimica Acta*, 2016, **218**, 32-40.
24. Y. J. Zhang, L. Ji, W. F. Li, Z. Zhang, L. Lu, L. S. Zhou, J. H. Liu, Y. Chen, L. W. Liu, W. Chen and Y. G. Zhang, *Journal of Power Sources*, 2016, **334**, 104-111.
25. L. L. Zhang, C. Yang, N. T. Hu, Z. Yang, H. Wei, C. X. Chen, L. M. Wei, Z. C. J. Xu and Y. F. Zhang, *Nano Energy*, 2016, **26**, 668-676.
26. Q. X. Xie, R. R. Bao, A. R. Zheng, Y. F. Zhang, S. H. Wu, C. Xie and P. Zhao, *ACS Sustain. Chem. Eng.*, 2016, **4**, 1422-1430.
27. V. H. Pham and J. H. Dickerson, *J. Phys. Chem. C*, 2016, **120**, 5353-5360.
28. G. X. Chen, S. L. Wu, L. W. Hui, Y. Zhao, J. L. Ye, Z. Q. Tan, W. C. Zeng, Z. C. Tao, L. H. Yang and Y. W. Zhu, *Scientific Reports*, 2016, **6**, 19028.
29. Y. L. Bai, X. F. Yang, Y. B. He, J. Y. Zhang, L. P. Kang, H. Xu, F. Shi, Z. B. Lei and Z. H. Liu, *Electrochimica Acta*, 2016, **187**, 543-551.
30. Y. X. Xu, C. Y. Chen, Z. P. Zhao, Z. Y. Lin, C. Lee, X. Xu, C. Wang, Y. Huang, M. I. Shakir and X. F. Duan, *Nano Lett.*, 2015, **15**, 4605-4610.
31. L. L. Jiang, L. Z. Sheng, C. L. Long, T. Wei and Z. J. Fan, *Adv. Energy Mater.*, 2015, **5**, 1500771.
32. D. Y. Guo, X. Chen, Z. P. Fang, Y. F. He, C. Zheng, Z. Yang, K. Q. Yang, Y. Chen and S. M. Huang, *Electrochim. Acta*, 2015, **176**, 207-214.
33. L. Jiang, L. Sheng, C. Long and Z. Fan, *Nano Energy*, 2015, **11**, 471-480.
34. Y. Xu, Z. Lin, X. Zhong, X. Huang, N. O. Weiss, Y. Huang and X. Duan, *Nat. Commun.*, 2014, **5**, 4554.
35. J. Luo, H. D. Jang and J. Huang, *ACS Nano*, 2013, **7**, 1464-1471.
36. X. Yang, C. Cheng, Y. Wang, L. Qiu and D. Li, *Science*, 2013, **341**, 534-537.
37. F. Shao, N. Hu, Y. Su, L. Yao, B. Li, C. Zou, G. Li, C. Zhang, H. Li, Z. Yang and Y. Zhang, *Chem. Eng. J.*, 2020, **392**, 123692.
38. Z. Li, S. Gadipelli, H. Li, C. A. Howard, D. J. L. Brett, P. R. Shearing, Z. Guo, I. P. Parkin and F. Li, *Nat. Energy*, 2020, **5**, 160-168.
39. H. Ma, H. Chen, M. Wu, F. Chi, F. Liu, J. Bai, H. Cheng, C. Li and L. Qu, *Angew. Chem. Int. Ed.*, 2020, **59**, 14541-14549.

40. H. Ma, H. Geng, B. Yao, M. Wu, C. Li, M. Zhang, F. Chi and L. Qu, *ACS Nano*, 2019, **13**, 9161-9170.
41. H. Banda, S. Perie, B. Daffos, P.-L. Taberna, L. Dubois, O. Crosnier, P. Simon, D. Lee, G. De Paepe and F. Duclairoir, *Acs Nano*, 2019, **13**, 1443-1453.
42. S. Zhang, J. Zhu, Y. Qing, L. Wang, J. Zhao, J. Li, W. Tian, D. Jia and Z. Fan, *Adv. Funct. Mater.*, 2018, **28**, 1805898.
43. P. Li, H. Li, D. Han, T. Shang, Y. Deng, Y. Tao, W. Lv and Q.-H. Yang, *Advanced Science*, 2019, **6**.
44. Y. H. Kim, B. H. Park, Y. J. Choi, G.-W. Lee, H.-K. Kim and K.-B. Kim, *Energy Storage Materials*, 2020, **24**, 351-361.
45. S. K. Kim, B. Lee, T. Ha, S.-R. Park, H. Chang, S. W. Lee and H. D. Jang, *Small*, 2018, **14**, 1801948.
46. Y. Jiang, J. Li, Z. Jiang, M. Shi, R. Sheng, Z. Liu, S. Zhang, Y. Cao, T. Wei and Z. Fan, *Carbon*, 2021, **175**, 281-288.
47. S. Herou, J. J. Bailey, M. Kok, P. Schlee, R. Jervis, D. J. L. Brett, P. R. Shearing, M. C. Ribadeneyra and M. Titirici, *Advanced Science*, 2021, 2100016.
48. J. Han, C. Zhang, D. Kong, X. He, J. Xiao, F. Chen, Y. Tao, Y. Wan and Q.-H. Yang, *Nano Energy*, 2020, **72**, 104729.
49. Y. Dong, S. Zhang, X. Du, S. Hong, S. Zhao, Y. Chen, X. Chen and H. Song, *Adv. Funct. Mater.*, 2019, **29**, 1901127.
50. C. Chen, M. Zhao, Y. Cai, G. Zhao, Y. Xie, L. Zhang, G. Zhu and L. Pan, *Carbon*, 2021, **179**, 458-468.